NANO LETTERS
Letter
Cite This: Nano Lett. 2019, 19, 2850−2857
pubs.acs.org/NanoLett

Increasing Photoluminescence Quantum Yield by Nanophotonic Design of Quantum-Confined Halide Perovskite Nanowire Arrays

Daquan Zhang,[†] Leilei Gu,[†] Qianpeng Zhang,[†] Yuanjing Lin,[†,‡] Der-Hsien Lien,[‡,§] Matthew Kam,[†] Swapnadeep Poddar,[†] Erik C. Garnett,[∥] Ali Javey,[‡,§] and Zhiyong Fan*[,†]

[†]Department of Electronic and Computer Engineering, The Hong Kong University of Science and Technology, Clear Water Bay, Kowloon, Hong Kong SAR, China
[‡]Electrical Engineering and Computer Sciences, University of California, Berkeley, California 94720, United States
[§]Materials Sciences Division, Lawrence Berkeley National Laboratory, Berkeley, California 94720, United States
[∥]Center for Nanophotonics, AMOLF, Science Park 104, 1098 XG Amsterdam, The Netherlands

Supporting Information

ABSTRACT: High-photoluminescence quantum yield (PLQY) is required to reach optimal performance in solar cells, lasers, and light-emitting diodes (LEDs). Typically, PLQY can be increased by improving the material quality to reduce the nonradiative recombination rate. It is in principle equally effective to improve the optical design by nanostructuring a material to increase light out-coupling efficiency (OCE) and introduce quantum confinement, both of which can increase the radiative recombination rate. However, increased surface recombination typically minimizes nanostructure gains in PLQY. Here a template-guided vapor phase growth of $CH_3NH_3PbI_3$ ($MAPbI_3$) nanowire (NW) arrays with unprecedented control of NW diameter from the bulk (250 nm) to the quantum confined regime (5.7 nm) is demonstrated, while simultaneously providing a low surface recombination velocity of 18 cm s^{-1}. This enables a 56-fold increase in the internal PLQY, from 0.81% to 45.1%, and a 2.3-fold increase in OCEy to increase the external PLQY by a factor of 130, from 0.33% up to 42.6%, exclusively using nanophotonic design.

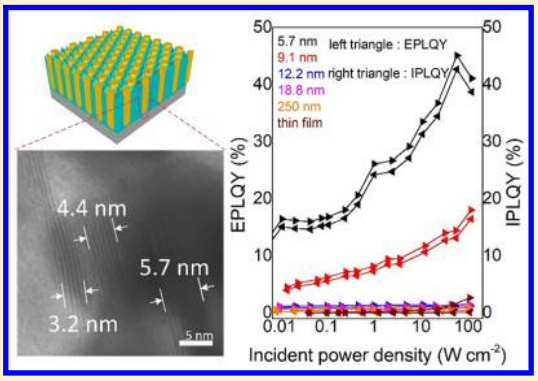

KEYWORDS: *Photoluminescence quantum yield, quantum confinement, perovskite, light out-coupling, photodetector*

The internal and external photoluminescence quantum yields (IPLQY and EPQLY) are defined as the ratio between the number of photons internally emitted and photons absorbed in the remote phosphor layer, and the ratio between the number of photons externally emitted and photons incident on the phosphor layer, separately. Considering the fact that IPLQY is determined by the relative rates of internal radiative and nonradiative recombination, which cannot be experimentally measured, it is thus more common to estimate it by using EPLQY and the light out-coupling efficiency (OCE). Hence, both the IPLQY and EPLQY play a key role in the performance of a wide variety of optoelectronic devices such as solar cells,[1,2] light-emitting diodes (LEDs),[3−5] and lasers.[6] The common approach to increase PLQY is to improve material quality, which reduces the nonradiative recombination rate, for example, by minimizing bulk,[7] surface,[8] and interfacial[9] defects. It is in principle also possible to increase PLQY solely via nanophotonic engineering, by increasing the absorption cross-section,[10] light out-coupling,[11] or quantum confinement.[12] All of these strategies increase the radiative recombination rate, but very often the increase in surface recombination when nanostructuring a material plays a bigger role, leading to an overall loss in PLQY. In the most successful example so far, nanostructuring InP increased PLQY by a factor of 14 using a combination of increased absorption cross-section and light out-coupling.[13] Such a large improvement was enabled by the very low native surface recombination velocity (SRV) of InP as well as its high refractive index, which leads to low OCE (2%) in planar wafers due to total internal reflection. Increasing light out-coupling has also been applied to halide perovskite materials, but the lower refractive index makes it more difficult to see an improvement; indeed only a factor of 3 has been observed so far.[14] However, halide perovskites also have very low native SRV,[15] making them an interesting candidate for studying radiative recombination rate enhancements via quantum confinement. Several studies have observed quantum confinement in colloidal halide perovskite nanowires (NWs).[16−19] In one case, smaller diameters led to lower PLQY, showing that surface recombination dominated over the quantum confinement effect.[16] In another example, a substantial increase in PLQY by a factor of 6 was observed,[17] but different synthetic conditions used to reach different NW

Received: December 6, 2018
Revised: March 14, 2019
Published: April 1, 2019

DOI: 10.1021/acs.nanolett.8b04887
Nano Lett. 2019, 19, 2850−2857

diameters made it difficult to determine the relative effect of quantum confinement versus differences in material quality. Furthermore, colloidal systems are not suitable for most optoelectronic applications, where quantum wires (QWs) need to be in the solid-state and in a geometry that allows for external contacting and efficient carry extraction/injection. It is thus an outstanding challenge to synthesize QWs with tunable diameters suitable for fundamental studies and optoelectronic device applications, while equally challenging is reaching sufficiently excellent surface passivation so that the change in radiative recombination rate rather than surface recombination dominates the PLQY.

Here we tackle both the synthetic and surface passivation challenges enabling a high IPLQY (45.1%) and a 130-fold increase in EPLQY only via reducing the NW diameter, by far the largest enhancement originating from quantum confinement and nanophotonic effects. We utilize porous alumina membranes (PAMs) as templates to fabricate ultrahigh density ($\sim 10^{12}$ cm^{-2}) vertical $CH_3NH_3PbI_3$ ($MAPbI_3$) NW arrays with controllable and uniform diameters from 250 ± 10 nm down to 5.7 ± 1.4 nm, all grown under the same vapor−solid−solid reaction (VSSR) conditions.[20−22] The processes for PAM formation, VSSR growth, photodetector fabrication, and extraction of QWs for transmission electron microscopy (TEM) characterization are shown schematically in Figure 1

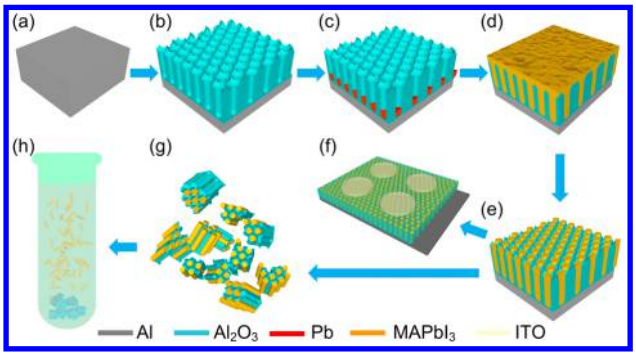

Figure 1. Schematic of PAM template-assisted growth of $MAPbI_3$ QW arrays for single QW extraction and photodetector fabrication.

(full details in Methods). Briefly, the nanoengineered PAMs are formed by electrochemical anodization of aluminum (Al) foil with the pore diameters in nanometers approximately equal to the anodization voltage in volts (Figures S1 and S2). Specifically, from the SEM images it can be seen that the nanopores are semiordered on substrate with diameters of 5.7 ± 1.4, 9.1 ± 1.0, 12.2 ± 1.8, and 18.8 ± 2.2 nm, respectively, which hence determine the diameters of both subsequently electrodeposited Pb NW precursor and the grown $MAPbI_3$ QWs. Meanwhile, the 5 V PAM has an ultrahigh pore density which can be calculated as high as $\sim 1 \times 10^{12}$ cm^{-2}. This unique feature of PAM will consequently contribute to ultrahigh density perovskite QW arrays with every single QW well isolated, which will be extremely promising for the ultrahigh resolution imaging or sensing applications in the future. After a barrier layer thinning process, metallic Pb is electrochemically deposited at the bottom of the PAM channels and subsequently converted to $MAPbI_3$ NW arrays using the VSSR process.[20] A variety of perovskite NWs can be obtained with a similar process simply by electrodepositing different metals at the bottom of the PAM or by using different powder precursors during the growth.[21,22] A low-energy surface ion-milling process is carried out to remove the unwanted layer of bulk polycrystalline $MAPbI_3$ on top of the PAM, leading to NWs with identical length in all PAM nanochannels. Afterward, another short growth step using the same conditions is applied to repair the ion beam damaged surface. All optical measurements are performed on the arrays at this stage (Figure 1e). For the photodetector measurements, patterned indium tin oxide (ITO) contacts are sputtered on top of the NW arrays without further annealing process (Figure 1f).

Our previous reports have confirmed that a PAM can serve as an excellent packaging material for halide perovskite NWs, leading to the drastically improved stability against water, oxygen, and spontaneous phase transformation.[20−22] This stability enhancement is critical for device applications, however also makes it difficult to extract individual NW for TEM characterization. Because etching away the PAM with acids/bases would destroy the perovskite NW array, we instead mechanically grind the embedded array into a fine powder (Figure 1g) and subsequently sonicate it in chlorobenzene. The sonication extracts the NWs from the broken edges of the PAM and uniformly disperses them in the solvent (Figure 1h), enabling TEM characterization as well as future single QWs device fabrication and characterization.

High-resolution TEM (HRTEM) and X-ray diffraction (XRD) confirm that the $MAPbI_3$ NWs are monocrystalline (Figure 2). Interestingly, the XRD patterns are dominated by (100) planes matching with the pattern of standard cubic $MAPbI_3$, indicating the NWs have a cubic crystal structure,[20,23] corresponding to the high-temperature phase (>327 K) of bulk $MAPbI_3$.[24] The reason for this stable cubic phase rather than the tetragonal phase at room temperature can be attributed to the spatial confinement of the PAM template, which has

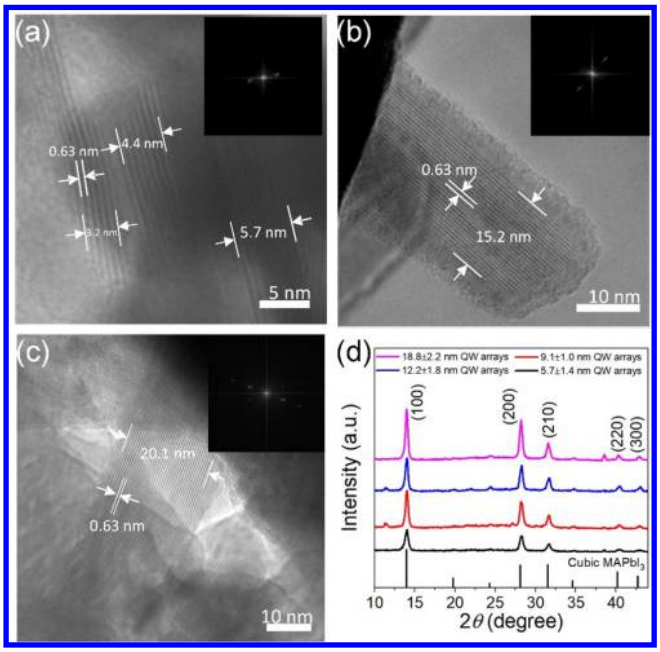

Figure 2. Crystal structure characterization of $MAPbI_3$ QWs. HRTEM images of $MAPbI_3$ QWs extracted from (a) 5, (b) 15, and (c) 20 V PAM. The insets show the corresponding FFT analysis. (d) XRD patterns of $MAPbI_3$ QW arrays in 5 V (black curve), 10 V (red curve), 15 V (blue curve), and 20 V (pink curve) PAM and standard cubic $MAPbI_3$.

DOI: 10.1021/acs.nanolett.8b04887
Nano Lett. 2019, 19, 2850−2857

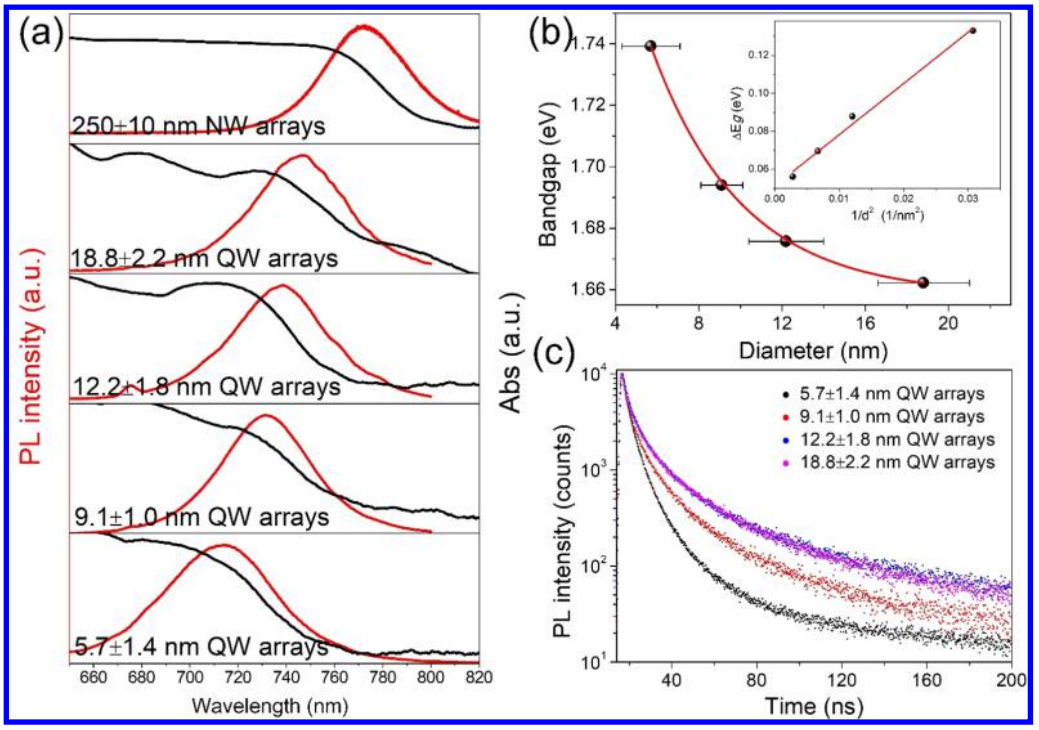

Figure 3. Optical properties characterization of $MAPbI_3$ QWs. (a) Normalized PL spectra (λ_{ex} = 400 nm) of $MAPbI_3$ QW arrays in different PAM templates and $MAPbI_3$ NW arrays, showing a maximum 59 nm PL peak blue shift. (b) Dependence of calculated bandgap on the QW diameter. The insert: the linear fitting of bandgap change versus $1/d^2$. (c) TRPL (λ_{ex} = 365 nm) measured at the PL peak for $MAPbI_3$ QWs with different diameters.

already been confirmed on $FAPbI_3$ and $CsPbI_3$ NWs growth.[22,25] More specifically, cubic phase $MAPbI_3$ can be naturally obtained during the high-temperature (180 °C) growth.[24] Then, after finishing the growth and cooling down to the room temperature, the PAM template provides spacial confinement that prevents perovskite NWs from lattice distortion and volume expansion which are required for the transformation to tetragonal phase. Hence, the cubic phase of perovskite NWs in the PAM template is eventually stabilized at room temperature. It has been reported that crystallite size of nanocrystals can be estimated with XRD result by using Scherrer equation[26]

$$D = \frac{0.89\lambda}{B\cos\theta} \tag{1}$$

where D is the average crystallite size, B and θ are, respectively, the full width at half-maximum (FWHM) and the angle of XRD peak, and λ is the wavelength of the X-ray (0.154056 nm). From XRD results in Figure 2d, the FWHM values of (100) peak for QWs with diameters of 5.7, 9.1, 12.2, and 18.8 nm are 0.474°, 0.385°, 0.383°, and 0.326°, respectively. Therefore, the crystallite size of these four kinds of QWs can be calculated as 16.7, 20.5, 20.7, and 24.3 nm. Compared with the extracted diameters from SEM, the larger size values calculated from XRD can be attributed to the fact that each individual QWs have different growth orientations.[20] This can also be seen from Figure 2d. When (100) plane are parallel to QW axial direction, the calculated crystallite size is equal to QW diameter. However, when (100) plane are perpendicular to QW axial direction, the calculated crystallite size is equal to QW length, namely 100 nm. Therefore, eventually the calculated nanocrystallite size is larger than the actual diameter of QWs. Nevertheless, the obvious decrease in signal intensity and comparative broadening of FWHM of the diffraction peaks is still consistent with the QW diameter reduction, as also observed in colloidal perovskite quantum dots (QDs)[27] and QWs.[16] From the HRTEM, it is clear that both the electrodeposited Pb and the converted $MAPbI_3$ NWs have the diameters determined entirely by the PAMs (Figures 2 and S3). The interplanar distance of ~0.63 nm corresponds to the (100) planes of cubic $MAPbI_3$, the same as observed in nanocrystals.[28]

The absorption and PL spectra show that the 250 nm diameter NW arrays exhibit optical properties comparable to those of bulk $MAPbI_3$ (Figure 3a),[20] while as the diameter decreases toward the Bohr radius, the PL peak and absorption edge show a significant blue shift, indicating bandgap widening due to quantum confinement. Especially, compared with the PL peak and absorption edge of 772 nm for 250 ± 10 nm diameter NW arrays, the 5.7 ± 1.4 nm diameter QW arrays show a maximum blue shift of 59 nm (133 meV). Note that recently a maximum 122 nm (301.5 meV) blue shift was observed from $MAPbI_3$ QDs with almost the same diameter (6.6 ± 0.7 nm).[29] This discrepancy can be explained by the fact that QWs have only two-dimensional (2D) confinement of excitons while QDs have three-dimensional (3D) confinement.[30] Figure 3b quantitatively illustrates the dependence of optical bandgaps on the average NW diameters, calculated using the PL peak positions. The bandgap change (ΔE_g) shows an inverse square relationship ($\Delta E_g \propto 1/d^2$) to the diameter (d), consistent with the simple particle-in-a-box model for QWs[30−32]

$$\Delta E_g = \frac{1.17h^2}{8d^2}\cdot\left(\frac{1}{m_e^*} + \frac{1}{m_h^*}\right) = \frac{1.17h^2}{8m^* d^2} = \frac{k}{d^2} \tag{2}$$

DOI: 10.1021/acs.nanolett.8b04887
Nano Lett. 2019, 19, 2850−2857

Table 1. Average Lifetimes (τ_{ave}), OCE, EPLQY, and IPLQY Values under ~50 W cm^{-2} Incident Power Density, Internal Radiative (R_{rad}) and Nonradiative (R_{nrad}) Recombination Rates for Different NW Arrays[a]

diameter (nm)	τ_{ave} (ns)	OCE (%)	EPLQY (%)	IPLQY (%)	internal R_{rad} ($\times 10^7$ s^{-1})	internal R_{nrad} ($\times 10^8$ s^{-1})
5.7	4.126	90.6	42.6	45.1	3.96	2.01
9.1	6.001	89.4	13.1	14.4	1.04	1.56
12.2	8.124	72.4	0.87	1.21	0.15	1.22
18.8	8.325	56.5	0.78	1.37	0.12	1.19
250	3.039	39.8	0.33	0.81	0.19	3.1

[a] τ_{ave} is extracted from the double-exponential fitting of PL decays with definition shown in Methods.

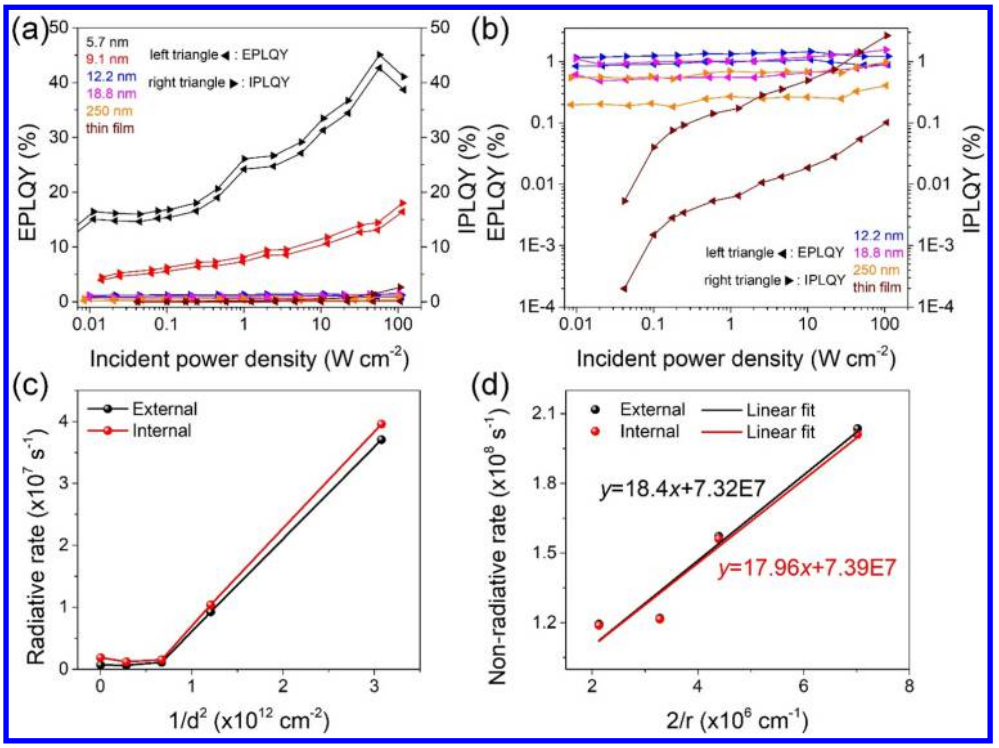

Figure 4. Optical properties characterization of $MAPbI_3$ QWs. Incident power density (λ_{ex} = 514 nm) dependent EPLQY and IPLQY values of QW arrays, NW arrays and thin film counterpart with (a) linear scale and (b) log scale. (c) External and internal radiative recombination rates versus the inverse NW diameter squared. (d) External and internal nonradiative recombination rate versus the nanowire surface-to-volume ratio ($2/r$).

where, h, m_e^*, m_h^*, and m^* represent Planck's constant and the electron, hole, and reduced effective mass, respectively. Using the slope value (k) of 2.70 eV nm^2 extracted from the linear fitting (Figure 3b inset), the reduced effective mass m^* is estimated to be $0.16m_0$, where m_0 is the free electron mass. This result is consistent with the reported value of $0.15m_0$.[33] Time-resolved photoluminescence (TRPL) measurements show that smaller diameter NWs have faster PL decays (see Methods fitting details), corresponding to shorter carrier lifetimes (Figure 3c, Table 1). Typically, shorter carrier lifetime suggests more carrier recombination. Because there are mainly two routes of recombination, namely, radiative and nonradiative recombination, increase of either or both recombination rate can lead to a shorter carrier lifetime. Organometal perovskite materials are known to have low bulk defects thus bulk defect-associated nonradiative recombination is low.[15] Meanwhile, recently we have discovered that our PAMs provide excellent surface passivation to perovskite NWs, thus SRV is very low.[34] One may consider that smaller QW diameter leads to larger surface-to-volume ratio and more severe surface nonradiative recombination, as observed in some inorganic NWs.[35,36] However, smaller diameter NWs provided much stronger spacial confinement to the photogenerated excitons, as compared with larger diameter NWs. This increases radiative recombination rate in the smaller diameter NWs, as also reported in QD materials.[37] Therefore, we can draw a conclusion that short carrier lifetime is caused by increasing radiative recombination. This argument can be further substantiated by the fact that the smaller diameter NWs/QWs have higher PLQY than large diameter NWs, which will be discussed below.

Figure 4a,b (left triangles) show that as the NW diameters decrease from 250 to 5.7 nm, the EPLQYs increase from 0.33% to 42.6%. In all cases, the EPLQYs are weakly dependent on excitation intensity with a maximum enhancement by a factor 4 when changing the power intensity by 4 orders of magnitude. This suggests all NW samples are in the low-injection regime, where the background carrier density is much higher than the photogenerated carrier density.[3] However, the situation is very different for the thin film, which not only shows a lower EPLQY (maximum of 0.1%) but also a strong power dependence, approaching the linear scaling expected for films dominated by nonradiative recombination in the high injection regime.[38] The large difference likely arises from the different

DOI: 10.1021/acs.nanolett.8b04887
Nano Lett. 2019, 19, 2850−2857

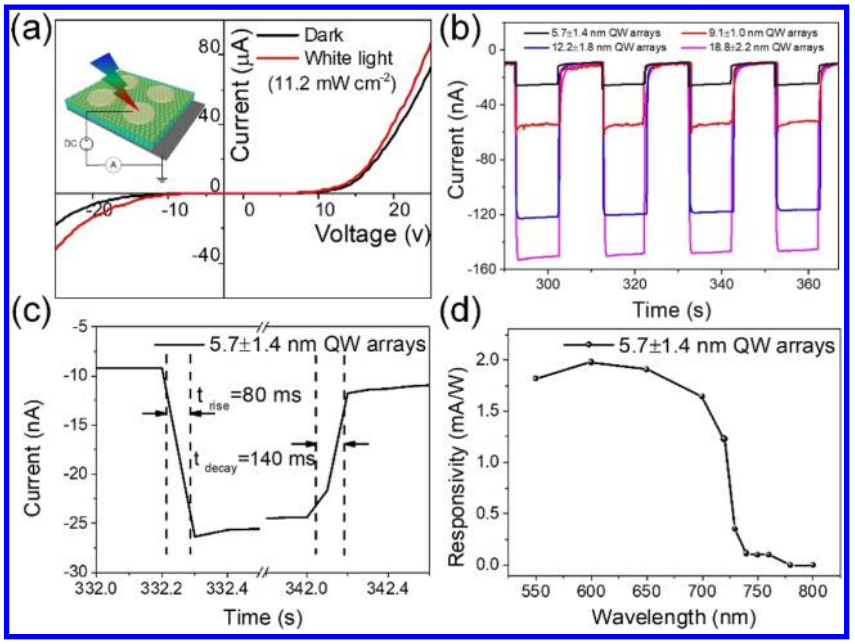

Figure 5. Optoelectronic properties characterization of $MAPbI_3$ QW arrays based photodetector devices. (a) $I-V$ curves under dark condition and white color light illumination (11.2 mW cm^{-2}) for 5.7 ± 1.4 nm QW arrays based device. (b) Time-domain photoresponses to the same white color light for different diameter $MAPbI_3$ QW arrays based devices under −5 V bias. (c) Response time under the same white light and (d) wavelength-dependent responsivity analysis for 5.7 ± 1.4 nm QW arrays based device with −5 V bias.

synthetic methods between the thin-film and NW arrays. The increase in PLQY with stronger quantum confinement suggests the origin of the improvement is an increased radiative recombination rate (nanophotonic effect), rather than a decreased nonradiative recombination rate (improved material quality). To obtain the IPLQY values, we first simulated the OCE of different dipoles polarizations (typically the vertical and horizontal dipoles) in the NW arrays using finite-difference time-domain (FDTD) method with simulation details and results shown in Supporting Information. However, a simple average of those two different polarization values, which is usually suitable for planar perovskite films,[39] is not the case in our QW arrays because the quantum confinement will bias the emission toward the dipole polarization direction with the strongest confinement and then alter the light out-coupling.[40] Hence, more precisely, we used the relative internal radiative recombination rate enhancement, which can be extracted by using the IPLQY and lifetime data, as the weighting factors for those two components. Then, a modified photon recycling model[14] was used to calculate the IPLQY with the use of EPLQY and OCE with calculation details shown in Supporting Information. Generally, compared with 250 nm NW arrays, the OCE for 5.7 nm QW arrays shows a 2.3 times enhancement from 39.8% to 90.6%, as shown in Table 1 and Figure S6. Figure 4a,b (right triangles) shows the power-dependent IPLQYs for different NW arrays and thin films. Significantly, the EPLQY (42.6%) for 5.7 nm QW arrays only show ∼5% lower than the IPLQY (45.1%) which is mainly attributed to the highly effective light out-coupling (90.6%). However, this reduction is as low as 60% for 250 nm NW arrays and 96% for thin films which confirms the expectation that reducing NW diameter will enhance the light out-coupling.[41] Figure 4c plots the internal and external radiative recombination rates versus the inverse NW diameter squared. The difference between those two rates shows the same trend with that of IPLQY. Meanwhile, above a diameter of 12 nm, the radiative recombination rate is nearly constant, while it increases linearly below this threshold diameter, ultimately reaching a value at 5.7 nm that is 54 times higher than that at 250 nm. As the NW diameter shrinks, we also expect the nonradiative recombination rate to boost due to the increased surface recombination.[42] Plotting the internal and external nonradiative recombination rates versus the NW surface-to-volume ratio ($2/r$) allows us to extract a consistent SRV of ∼18 cm s^{-1} from the slope of the linear fits (Figure 4d),[34] which is rather low for perovskite materials.[43] The strong confinement of the templates-induced superstability of QWs over NWs and thin films are also demonstrated (Figure S5).

High-quality perovskite materials with superior properties and stability are promising for optoelectronic device applications such as photodetectors with tunable spectral response.[20−22,44] However, due to the material stability issue and incompatibility with nanofabrication processes, device fabrication using individual perovskite QWs remains a challenge. Our ultrahigh density (∼10^{12} cm^{-2}) vertical QW arrays can be simply integrated with contacts to fabricate photodetectors, as shown in the inset of Figure 5a. In such a device, the Al substrate and the layer of 100 nm transparent ITO film (100 Ω/□), which was sputtered without further annealing process, serve as the bottom and top electrodes, respectively. Figure S7 shows the transmittance of 100 nm ITO thin film sputtered on glass substrate. The schematic energy band diagrams for zero, forward, and reverse biases are shown in Figure S8. Under zero bias, the photogenerated electron-hole pairs cannot be easily collected by the electrodes because of the existence of the Al_2O_3 barrier layer between the Al electrode and the QWs. However, when applying high enough bias, carriers can gain enough energy from internal field and tunnel through the barrier layer thus leading to a large tunneling current. This asymmetric contact structure leads to a Schottky junction, which can be observed in the $I-V$ curves

DOI: 10.1021/acs.nanolett.8b04887
Nano Lett. 2019, 19, 2850−2857

under dark and white halogen light (11.2 mW cm^{-2}) illumination (Figures 5a and S9). Note that in negative bias condition, electrons are required to overcome the energy barrier $E_{b1} \sim 0.8$ eV between ITO Fermi level and perovskite conduction band to sustain a continuous current flow. However, in the forward bias condition, electron injection energy barrier height E_{b2} between perovskite and Al_2O_3/Al is much lower. Therefore, forward bias current is much higher than the reverse bias current, as shown in Figure 5a. Figure 5b characterizes the time-domain light response under −5 V bias and pulsed white light (11.2 mW cm^{-2}) for different QW arrays. The stable photocurrent drops from ∼140 to ∼16 nA when decreasing the QWs diameter from 18.8 ± 2.2 to 5.7 ± 1.4 nm, which can be attributed to the photocarrier loss via increased radiative recombination as discussed before. Namely, under the same optical and electrical condition, more photogenerated electron-hole pairs recombine with each other and hence emit the light rather than being collected by two electrodes in the smaller QWs device. In the future, the photoresponse can be further enhanced by using shorter QWs and by removing Al_2O_3 barrier layer completely.[20] The typical response time of the device are extracted from the $I-t$ curve shown in Figure 5c. The photocurrent rise time (t_{rise}) of 80 ms and fall time (t_{fall}) of 140 ms are reasonably short and can be further improved by shortening the QW length to reduce the resistance and charge-carrier collection time and by shrinking the top electrode area to reduce the parasitic capacitance between the two electrodes. The wavelength-dependent responsivity is characterized and shown in Figure 5d with the input optical spectrum shown in Figure S10. In this case, the 5.7 ± 1.4 nm QW array device was used for measurement and the same −5 V bias was applied. It can be seen that the photoresponsivity has a peak value of ∼2 mA W^{-1} and suddenly drops from 1.23 mA W^{-1} to ∼0 when the incident optical wavelength increases from 720 to 730 nm, which is in excellent agreement with the absorption edge and PL emission peak shown in Figure 3a.

In this work, we demonstrate intriguing quantum confinement and nanophotonic effects in perovskite QW arrays. Particularly, quantum confinement results in 56-fold enhancement in IPLQY and nanophotonic effect contributes to 2.3-fold increase in light out-coupling, when NW diameter shrinks from bulk (250 nm) to quantum confined regime (5.7 nm). Together these two effects lead to a 130-fold substantial boost in EPLQY for QWs versus bulk NWs. In addition, it is also discovered that the QWs have a low SRV of 18 cm s^{-1} which is comparable to state-of-the-art well passivated Si, and it is a necessary enabling condition to observe the enormous PLQY improvement. The QWs have been fabricated into photodetectors to demonstrate the ease of electrical contact for optoelectronic devices. Furthermore, the photoresponse is found to be dependent on QW diameters due to quantum confinement as well. Together with good QW stability embedded in alumina template, the fabricated QWs may find potential applications in high performance and highly integrated optoelectronics in the future.

Methods. *PAM Fabrication.* The PAMs were fabricated by using a well-known anodic anodization with low voltages. Briefly, after being cleaned with acetone and isopropyl alcohol, a high purity Al foil with around 1.5 × 2.5 cm^2 size was electrochemically polished in an acidic solution made from 25 vol % $HClO_4$ and 75 vol % CH_3CH_2OH for 2.5 min under 12.5 V at room temperature. Afterward, the first anodic anodization was carried out by immersing the Al chip into acid solution (5 vol % H_2SO_4) under different direct current (dc) voltages (5, 10, 15, and 20 V) at 10 °C for different times (24, 12, 5, and 3 h), respectively. Followed by the second anodization with the same condition, an acid etching (6 wt % H_3PO_4 and 1.8 wt % CrO_3) of the first anodization layer was carried out at 98 °C for 15 min. To get 100 nm thick PAM in the second anodization, it empirically took around 20, 10, 2, and 1 min for 5, 10, 15, and 20 V anodization, respectively. At the end of the second anodization (except for the 5 V one), the dc voltage source mode was directly switched to dc current source mode with current value being half of that in voltage mode, which would trigger a voltage-ramping-down process and hence thin down the barrier layer at the bottom of PAM channels. When the voltage reached 5 V, the process was terminated and the PAM chips were rinsed with deionized (DI) water and dried with compressed air for the later use.

Pb Electrodeposition. The Pb precursor was electrochemically deposited at the bottom of PAM nanochannels in aqueous electrolyte made from 1.7 g of $PbCl_2$, 25 g of trisodium citrate and 100 mL of DI water. A potentiostat (Series G-300, Gamry instruments) was used to supply a sinusoidal voltage signal with 60 Hz frequency and 5 V amplitude for 10 s. Nanocrystalline Pb NWs would be consequently obtained at the bottom of PAM channels.

$MAPbI_3$ QWs Growth and Photodetector Device Fabrication. The $MAPbI_3$ QWs were synthesized through the reaction between Pb and MAI vapor as reported earlier.[20] Briefly, the PAM chip with Pb NWs deposited was placed into the face-to-face glass bottles with MAI powder inside, which helps to trap the MAI vapor and hence promotes the reaction. A tube furnace (1 in. diameter size) with Ar carrier gas was then used to heat them up to 180 °C for 5 min to completely consume Pb precursor. To guarantee all QWs having identical length, excess Pb precursor was deposited beforehand to make sure there is a layer of $MAPbI_3$ thin film on the top surface of PAM template, and successively a surface ion milling process and regrowth were carried out to remove the polycrystalline thin film. Specifically, in the 1 h ion milling process argon ions were accelerated by 100 V voltage in a vacuum of 1.4 × 10^{-4} Torr. The angle between the ion acceleration path and the normal of the chip is 80° with continuous rotation of the chip during the etching. Afterward, another VSSR process with the same growth condition was carried out but only for 30 s to repair the ion beam damaged surface. To fabricate a photodetector device, a transparent 100 nm layer of ITO was sputtered on top of the substrate without further annealing process using a circle shadow mask of 0.0314 cm^2 area.

Single Pb NW and $MAPbI_3$ QW Extraction. To extract a single $MAPbI_3$ QW out from the PAM template for TEM, a mechanical grinding and sonication process was utilized. Followed by the $MAPbI_3$ QWs growth, a free-standing PAM membrane with deposited Pb NWs was obtained by $HgCl_2$ etching.[20] Afterward, the membrane was mechanically ground into fine powder, dispersed in chlorobenzene, and sonicated for 20 min, which finally would extract QWs out from the edge of broken PAM pieces and uniformly disperse them into the solvent. The Pb NWs extraction was carried out by using the same process except for the $MAPbI_3$ QWs growth step.

Characterization. SEM images of PAM were characterized using a field-emission scanning electron microscopy (JEOL JSM-7800F). XRD patterns of $MAPbI_3$ QW arrays in PAM were obtained using Bruker D8 X-ray diffractometer. TEM

DOI: 10.1021/acs.nanolett.8b04887
Nano Lett. 2019, 19, 2850−2857

images were obtained by TEM JEOL (2010) with 200 kV acceleration voltage. UV−vis absorption and PL including spectrum and lifetime were measured using Varian Cary 500 spectrometer (Varian, U.S.A.) and Edinburgh FS5 fluorescence spectrometer, respectively. The PLQY was measured using a custom-built micro-PL instrument reported by us before with more details in the Supporting Information.[45] A double-exponential function was used to fit all PL decay profiles

$$I(t) = A + B_1 e^{(-t/\tau_1)} + B_2 e^{(-t/\tau_2)} \quad (3)$$

with fitting results shown in Table S1. The average lifetime (used to calculate radiative and nonradiative recombination rates) is given by $\tau_{ave} = \frac{\tau_1 * B_1 + \tau_2 * B_2}{B_1 + B_2}$.

The photodetector device was characterized using a HP 4156A Analyzer along with probe station (Sigatone, U.S.A.) and broadband Halogen lamp as a light source.

Simulation. The time domain light out coupling efficiency simulation for $MAPbI_3$ NW arrays and thin film counterpart was performed using Lumerical FDTD software package. All the NW arrays and thin film were 100 nm thick. Refractive index for perovskite is $n = 2.6$, $k = 0.2$.[46] Refractive index for Al_2O_3 is using the "Al_2O_3−Palik" in the inset material database. Dipole light sources with horizontal and vertical polarizations were used to simulate the isotropic light-generation process. Source wavelength were 713, 732, 740, 746, 772, and 772 nm for 5.7, 9.1, 12.2, 18.8, 250 nm NW arrays and thin film sample. Periodic boundary conditions were applied on the *x*- and *y*-directions. Then the light out coupling efficiency was extrapolated by the ratio of the far-field light power over the light source power. Cross-sectional *E* field monitors and time monitors were added to record the *E* field intensity distribution and light propagation.

■ ASSOCIATED CONTENT

Supporting Information

The Supporting Information is available free of charge on the ACS Publications website at DOI: 10.1021/acs.nanolett.8b04887.

Time domain light (713 nm) extraction process in 5.7 ± 1.4 nm $MAPbI_3$ NW arrays (MPG)

Time domain light (732 nm) extraction process in 9.1 ± 1.0 nm $MAPbI_3$ NW arrays (MPG)

Time domain light (740 nm) extraction process in 12.2 ± 1.8 nm $MAPbI_3$ NW arrays (MPG)

Time domain light (746 nm) extraction process in 18.8 ± 2.2 nm $MAPbI_3$ NW arrays (MPG)

Time domain light (772 nm) extraction process in 250 ± 10 nm $MAPbI_3$ NW arrays (MPG)

Time domain light (772 nm) extraction process in $MAPbI_3$ thin film (MPG)

AAO pore size distribution, TEM images of Pb NWs and $MAPbI_3$ QWs, PLQY measurement setup and method, stability test for QWs, NWs and thin films, dynamic QW arrays PL profiles fitting, light out-coupling efficiency simulation, iterative calculation of IPLQY using measured EPLQY and simulated light out-coupling efficiency, transmittance of ITO film, photodetector device physics and performance (PDF)

■ AUTHOR INFORMATION

Corresponding Author

*E-mail: eezfan@ust.hk.

ORCID

Zhiyong Fan: 0000-0002-5397-0129

Notes

The authors declare no competing financial interest.

■ ACKNOWLEDGMENTS

This work was supported by the National Natural Science Foundation of China (Project 51672231) and the General Research Fund (Project Nos. 612113 and 16237816) from the Hong Kong Research Grant Council. The authors acknowledge the support received from the Center for 1D/2D Quantum Materials and State Key Laboratory on Advanced Displays and Optoelectronics at HKUST. The PLQY measurements were performed in the Electronic Materials program funded by the Director, Office of Science, Office of Basic Energy Sciences, Materials Sciences and Engineering Division of the U.S. Department of Energy, under contract no. DE-AC02-05Ch11231. D.Z. acknowledges the technical assistance from Miss Jenny Kontoleta from Center for Nanophotonics, AMOLF Amsterdam, The Netherlands.

■ REFERENCES

(1) Akkerman, Q. A.; Gandini, M.; Stasio, F. D.; Rastogi, P.; Palazon, F.; Bertoni, G.; Ball, J. M.; Prato, M.; Petrozza, A.; Manna, L. *Nat. Energy* **2017**, *2*, 16194.

(2) Carey, G. H.; Abdelhady, A. L.; Ning, Z. J.; Thon, S. M.; Bakr, O. M.; Sargent, E. H. *Chem. Rev.* **2015**, *115*, 12732.

(3) Yuan, M. J.; Quan, L. N.; Comin, R.; Walters, G.; Sabatini, R.; Voznyy, O.; Hoogland, S.; Zhao, Y. B.; Beauregard, E. M.; Kanjanaboos, P.; Lu, Z. H.; Kim, D. H.; Sargent, E. H. *Nat. Nanotechnol.* **2016**, *11*, 872.

(4) Chiba, T.; Hayashi, Y.; Ebe, H.; Hoshi, K.; Sato, J.; Sato, S.; Pu, Y. J.; Ohisa, S.; Junji, K. *Nat. Photonics* **2018**, *12*, 681.

(5) Lin, K. B.; Quan, L. N.; Arquer, F. P. G.; Gong, X. W.; Lu, J. X.; Xie, L. Q.; Zhao, W. J.; Zhang, D.; Yan, C. Z.; Li, W. Q.; Liu, X. Y.; Lu, Y.; Kirman, J.; Sargent, E. H.; Xiong, Q. H.; Wei, Z. H.; et al. *Nature* **2018**, *562*, 245.

(6) Veldhuis, S. A.; Boix, P. P.; Yantara, N.; Li, M. J.; Sum, T. C.; Mathews, N.; Mhaisalkar, S. G. *Adv. Mater.* **2016**, *28*, 6804.

(7) Shi, D.; Adinolfi, V.; Comin, R.; Yuan, M. J.; Alarousu, E.; Buin, A.; Chen, Y.; Hoogland, S.; Rothenberger, A.; Katsiev, K.; Losovyj, Y.; Zhang, X.; Dowben, P. A.; Mohammed, O. F.; Sargent, E. H.; Bakr, O. M. *Science* **2015**, *347*, 519.

(8) Marino, E.; Kodger, T. E.; Crisp, R. W.; Timmerman, D.; MacArthur, K. E.; Heggen, M.; Schall, P. *Angew. Chem.* **2017**, *129*, 13983.

(9) Chen, M. X.; Liu, Y.; Li, C. C.; Li, A.; Chang, X. X.; Liu, W.; Sun, Y.; Wang, T.; Gong, J. L. *Energy Environ. Sci.* **2018**, *11*, 2025.

(10) Xu, W. W.; Hou, X. Q.; Meng, Y. J.; Meng, R. Y.; Wang, Z. Y.; Qin, H. Y.; Peng, X. G.; Chen, X. W. *Nano Lett.* **2017**, *17*, 7487.

(11) Lien, D. H.; Kang, J. S.; Amani, M.; Chen, K.; Tosun, M.; Wang, H. P.; Roy, T.; Eggleston, M. S.; Wu, M. C.; Dubey, M.; Lee, S. C.; He, J. H.; Javey, A. *Nano Lett.* **2015**, *15*, 1356.

(12) Buhro, W.; Colvin, V. *Nat. Mater.* **2003**, *2*, 138.

(13) Cui, Y.; Dam, D. V.; Mann, S. A.; Hoof, N. J. J. V.; Veldhoven, P. J. V.; Garnett, E. C.; Bakkers, E. P. A. M.; Haverkort, J. E. M. *Nano Lett.* **2016**, *16*, 6467.

(14) Richter, J. M.; Abdi-Jalebi, M.; Sadhanala, A. S.; Tabachnyk, M.; Rivett, J. P. H.; Pazos-Outón, L. M.; Gödel, K. C.; Price, M.; Deschler, F.; Friend, R. H. *Nat. Commun.* **2016**, *7*, 13941.

(15) Yang, Y.; Yan, Y.; Yang, M. J.; Choi, S.; Zhu, K.; Luther, J. M.; Beard, M. C. *Nat. Commun.* **2015**, *6*, 7961.

DOI: 10.1021/acs.nanolett.8b04887
Nano Lett. 2019, 19, 2850−2857

(16) Teunis, M.; Jana, A.; Dutta, P.; Johnson, M.; Mandal, M.; Muhoberac, B.; Sardar, R. *Chem. Mater.* **2016**, *28*, 5043.
(17) Imran, M.; Stasio, F.; Dang, Z.; Canale, C.; Khan, A.; Shamsi, J.; Brescia, R.; Prato, M.; Manna, L. *Chem. Mater.* **2016**, *28*, 6450.
(18) Zhang, D. D.; Yu, Y.; Bekenstein, Y.; Wong, A. B.; Alivisatos, A. P.; Yang, P. D. *J. Am. Chem. Soc.* **2016**, *138*, 13155.
(19) Liu, Z. X.; Mi, Y.; Guan, X. W.; Su, Z. C.; Liu, X. F.; Wu, T. *Adv. Opt. Mater.* **2018**, *6*, 1800413.
(20) Gu, L. L.; Tavakoli, M.; Zhang, D. Q.; Zhang, Q. P.; Waleed, A.; Xiao, Y.; Tsui, K.; Lin, Y. J.; Liao, L.; Wang, J. N.; Fan, Z. Y. *Adv. Mater.* **2016**, *28*, 9713.
(21) Waleed, A.; Tavakoli, M.; Gu, L. L.; Wang, Z. Y.; Zhang, D. Q.; Manikandan, A.; Zhang, Q. P.; Zhang, R.; Chueh, Y.; Fan, Z. Y. *Nano Lett.* **2017**, *17*, 523.
(22) Waleed, A.; Tavakoli, M.; Gu, L. L.; Hussain, S.; Zhang, D. Q.; Poddar, S.; Wang, Z. Y.; Zhang, R. J.; Fan, Z. Y. *Nano Lett.* **2017**, *17*, 4951.
(23) Burschka, J.; Pellet, N.; Moon, S.-J.; Humphry-Baker, R.; Gao, P.; Nazeeruddin, M.; Grätzel, M. *Nature* **2013**, *499*, 316.
(24) Singh, R. K.; Kumar, A.; Jain, N.; Singh, J.; Singh, R. K.; Kumar, R. *Mater. Today: Proc.* **2017**, *4*, 12661.
(25) Gu, L. L.; Zhang, D. Q.; Kam, M.; Zhang, Q. P.; Poddar, W.; Fu, Y.; Mo, X. L.; Fan, Z. Y. *Nanoscale* **2018**, *10*, 15164−15172.
(26) Park, K.; Xiao, F.; Yoo, B. Y.; Rheem, Y.; Myung, N. V. *J. Alloys Compd.* **2009**, *485*, 362.
(27) Zhang, F.; Zhong, H.; Chen, C.; Wu, X.; Huang, H.; Han, J.; Zou, B.; Dong, Y.; et al. *ACS Nano* **2015**, *9*, 4533.
(28) Zushi, M.; Suzuki, A.; Akiyama, T.; Oku, T. *Chem. Lett.* **2014**, *43*, 916.
(29) Zhang, F.; Huang, S.; Wang, P.; Chen, X.; Zhao, S.; Dong, Y.; Zhong, H. *Chem. Mater.* **2017**, *29* (2017), 3793−3799.
(30) Yu, H.; Li, J.; Loomis, R.; Wang, L.; Buhro, W. *Nat. Mater.* **2003**, *2*, 517.
(31) Gudiksen, M.; Wang, J.; Lieber, C. *J. Phys. Chem. B* **2002**, *106*, 4036.
(32) Nanda, K.; Kruis, F.; Fissan, H. *Nano Lett.* **2001**, *1*, 605.
(33) Tanaka, K.; Takahashi, T.; Ban, T.; Kondo, T.; Uchida, K.; Miura, N. *Solid State Commun.* **2003**, *127*, 619.
(34) Khoram, P.; Oener, S. Z.; Zhang, Q. P.; Fan, Z. Y.; Garnett, E. C. *Mol. Syst. Des. Eng.* **2018**, *3*, 723.
(35) Liao, Z.; Zhang, H.; Zhou, Y.; Xu, J.; Zhang, J.; Yu, D. *Phys. Lett. A* **2008**, *372* (24), 4505−4509.
(36) Joyce, H. J.; Docherty, C. J.; Gao, Q.; Tan, H. H.; Jagadish, C.; LIoyd-Hughes, J.; Herz, L. M.; Johnston, M. B. *Nanotechnology* **2013**, *24* (21), 214006.
(37) Zhang, F.; Zhong, H.; Chen, C.; Wu, X.; Huang, H.; Han, J.; Zou, B.; Dong, Y.; et al. *ACS Nano* **2015**, *9* (4), 4533−4542.
(38) Yamada, Y.; Nakamura, T.; Endo, M.; Wakamiya, A.; Kanemitsu, Y. *J. Am. Chem. Soc.* **2014**, *136*, 11610.
(39) Cao, Y.; Wang, N. N.; Tian, H.; Guo, J. S.; Wei, Y. Q.; Chen, H.; Miao, Y. F.; Zou, W.; Pan, K.; He, Y. R.; Cao, H.; Ke, Y.; Xu, M. M.; Wang, Y.; Yang, M.; Du, K.; Fu, Z. W.; Kong, D. C.; Dai, D. X.; Jin, Y. Z.; Li, G. Q.; Li, H.; Peng, Q. M.; Wang, J. P.; Huang, W. *Nature* **2018**, *562*, 249.
(40) Novotny, L.; Hecht, B. *Principles of Nano-Optics*, 2nd ed.; Camrbidge University Press: New York, 2012.
(41) Babinec, T. M.; Hausmann, B. J. M.; Khan, M.; Zhang, Y. N.; Maze, J. R.; Hemmer, P. R.; Lončar, M. *Nat. Nanotechnol.* **2010**, *5*, 195.
(42) Dan, Y. P.; Seo, K.; Takei, K.; Meza, J. H.; Javey, A.; Crozier, K. B. *Nano Lett.* **2011**, *11*, 2527.
(43) Wu, B.; Nguyen, H. T.; Ku, Z. L.; Han, G. F.; Giovanni, D.; Mathews, N.; Fan, H. J.; Sum, T. C. *Adv. Energy Mater.* **2016**, *6*, 1600551.
(44) Zhang, Y.; Xu, W. X.; Xu, X. J.; Cai, J.; Yang, W.; Fang, X. S. *J. Phys. Chem. Lett.* **2019**, *10*, 836−841.
(45) Amani, M.; Lien, D.-H.; Kiriya, D.; Xiao, J.; Azcatl, A.; Noh, J. Y.; Madhvapathy, S. R.; Addou, R.; KC, S.; Dubey, M.; Cho, K.; Wallace, R. M.; Lee, S.-C.; He, J.-H.; Ager, J. W., lll; Zhang, X.; Yablonovitch, E.; Javey, A. *Science* **2015**, *350*, 1065.
(46) Zhang, Q. P.; Tavakoli, M. M.; Gu, L. L.; Zhang, D. Q.; Tang, L.; Gao, Y.; Guo, J.; Lin, Y. L.; Leung, S. F.; Poddar, S.; Fu, Y.; Fan, Z. Y. *Nat. Commun.* **2019**, *10*, 727.

DOI: 10.1021/acs.nanolett.8b04887
Nano Lett. 2019, 19, 2850−2857